Laser-Induced Regeneration of Spent $LiMn_2O_4$ Cathode into High-Performance Ni-Doped $LiMn_2O_4$ Cathode

Xucun Ye,[1] *Xiangyu Fei,*[2] *Mengjie Liu,*[1] *Hui Gao,*[1] *Baolong Qiu,*[1,3] *Huayi Yin,*[3] *Zhonghua Zhang,*[2,*] *and Lawrence Yoon Suk Lee*[1,*]

[1] Department of Applied Biology and Chemical Technology and Research Institute for Smart Energy, The Hong Kong Polytechnic University, Hung Hom, Kowloon, Hong Kong SAR, China

[2] Key Laboratory for Liquid-Solid Structural Evolution and Processing of Materials, School of Materials Science and Engineering, Shandong University, Jingshi Road 17923, Jinan 250061, China

[3] Key Laboratory for Ecological Metallurgy of Multimetallic Mineral of Ministry of Education, School of Metallurgy, Northeastern University, Shenyang 110819, China

* Corresponding authors: zh_zhang@sdu.edu.cn (Z. Zhang); lawrence.ys.lee@polyu.edu.hk (L. Y. S. Lee)

Abstract

The rapid increase in lithium-ion battery (LIB) production, fueled by the rise of electric vehicles, highlights significant challenges in managing end-of-life LIBs, particularly regarding environmental impact and waste management. Traditional recycling methods, such as pyrometallurgical and hydrometallurgical processes, are energy-intensive and consume substantial reagents. In this study, we introduce a laser-assisted regeneration method for $LiMn_2O_4$ (LMO) cathodes, enabling *in situ* Ni doping into spent LMO cathodes (r-LMO-Ni) to enhance electrochemical performance. Surface Ni-doping improves interfacial processes and reduces capacity loss at lower temperatures by creating a new interface with a lower charge transfer energy barrier. The r-LMO-Ni cathode surpasses pristine LMO cathodes, achieving a specific capacity of 112.95 mA h g^{-1} at 1 C and retaining 95.1 % of its capacity after 200 cycles at 0 °C. A techno-economic analysis supports the feasibility of this laser-assisted regeneration approach, offering an innovative pathway for upcycling spent cathodes and developing next-generation Mn-based cathodes.

Keywords: waste lithium-ion batteries; $LiMn_2O_4$ cathode; direct regeneration; laser ablation; low-temperature performance

1. Introduction

Surging global efforts to curb carbon emissions have fueled a dramatic increase in lithium-ion battery (LIB) production to meet the demands of electric vehicles, portable electronics, and energy storage systems.[1–3] This has inevitably led to a growing challenge of managing the increasing volume of decommissioned LIBs, typically after a lifespan of 5 to 10 years.[4] Implementing proper disposal and recycling protocols for these waste LIBs is critical to safeguard public health and the environment.[5] Decommissioned LIBs can considered as "urban mines" due to their high concentration of key metals, far exceeding those found in natural mineral ores by several magnitudes.[6,7] This presents a significant opportunity to enhance resource security and stabilize the supply chain for Li and transition metals through effective recycling and reuse strategies.[8,9] In addition to resource concerns, recycling LIB cathodes offers a cost-effective and environmentally friendly alternative to the production of virgin material production through mineral smelting, thus contributing to carbon neutrality goals.[10,11] However, conventional pyro- and hydrometallurgical recycling techniques face limitations that hamper their widespread adoption.[12–16] These methods are energy-intensive, require large quantities of chemicals, and generate hazardous waste streams that pose health and environmental risks if not properly managed.[17–19] While green recycling methods, such as electrochemistry-assisted methods, provide alternatives, they also come with challenges.[20–22] For example, while electrochemical oxidation effectively recovers Li, electrochemical reduction performs poorly in recycling transition metals with lower valence states.[23–26] Additionally, these techniques often suffer from low recovery rates, yielding only a fraction of the valuable metals while producing significant residual waste.[27–29] Thus, developing efficient and sustainable recycling methods is essential to ensure a stable supply of raw materials and to minimize the environmental impact associated with LIBs wastes.[30–32]

The Li deficiency theory, initially proposed by Kim *et al.* to explain the degradation of $LiCoO_2$ (LCO) cathode, uncovered an intrinsic mechanism for capacity fading.[33] This concept has been extended to the direct regeneration of degraded cathodes such as $LiMn_2O_4$ (LMO), $LiFePO_4$ (LFP), and $LiNi_xCo_yMn_zO_2$ (NCM).[34–36] Various techniques, including molten salt,[31] solid-state sintering,[36,37] and hydrothermal methods,[38] have been explored to address capacity decay caused by irreversible Li loss. These approaches aim to reintroduce Li ions into the deteriorated cathode lattice, restoring and restoring its capacity.[37,39–43] However, recent research have revealed an additional challenge: the irreversible dissolution of transition metals in LIB cathodes, which significantly impacts their electrochemical performance. To date, limited research has been conducted on the influence of transition metal loss in degraded and Li-restored cathodes.[36,37,44]

For LMO cathodes, Jahn−Teller distortion and Mn dissolution are primarily driven by enhanced local charge density along the z-axis direction due to orbital rearrangement in high-spin Mn^{3+} species.[45–47] This presents a significant hurdle for directly regenerating spent LMO (s-LMO) electrodes, as both Li and Mn vacancies must be addressed simultaneously. Recently, it has been demonstrated that incorporating Ni atoms into the LMO crystal structure, specifically by occupying Mn sites, creates a new interface with a reduced energy barrier for charge transfer.[48] Moreover, the formation of a more stable Ni–O bond can suppress the Jahn–Teller distortion, preventing Mn dissolution.[46]

Herein, we propose a novel strategy for regenerating s-LMO cathodes and enhancing their specific capacity and stability at low temperatures by simultaneously refilling Li and Ni atoms into the vacant sites of s-LMO using the pulsed laser ablation in liquid (PLAL) method. PLAL involves the initial destruction of s-LMO particles into plasma, followed by rapid quenching in a liquid containing Li and Ni ions. This process repairs both Li and Mn vacancies in s-LMO while concurrently doping its surface with Ni atoms. Our comprehensive structural analysis and theoretical calculations indicate that the introduction of Ni alters the internal chemical environment of the Mn octahedron, leading to the suppression of Mn migration and dissolution. Furthermore, surface-doped Ni lowers the energy barrier for charge transfer at the electrode interface. Consequently, the regenerated s-LMO exhibits remarkable low-temperature performance, retaining 95.1 % capacity at 1 C after 200 cycles at 0 °C. By simultaneously addressing Li and transition metal deficiencies, this work paves the way for a more sustainable approach to LIB regeneration, advancing a closed-loop and environmentally benign waste management strategy for LIBs.

2. Results and Discussion

2.1. Degradation Mechanism and Regeneration Process of LMO Cathodes

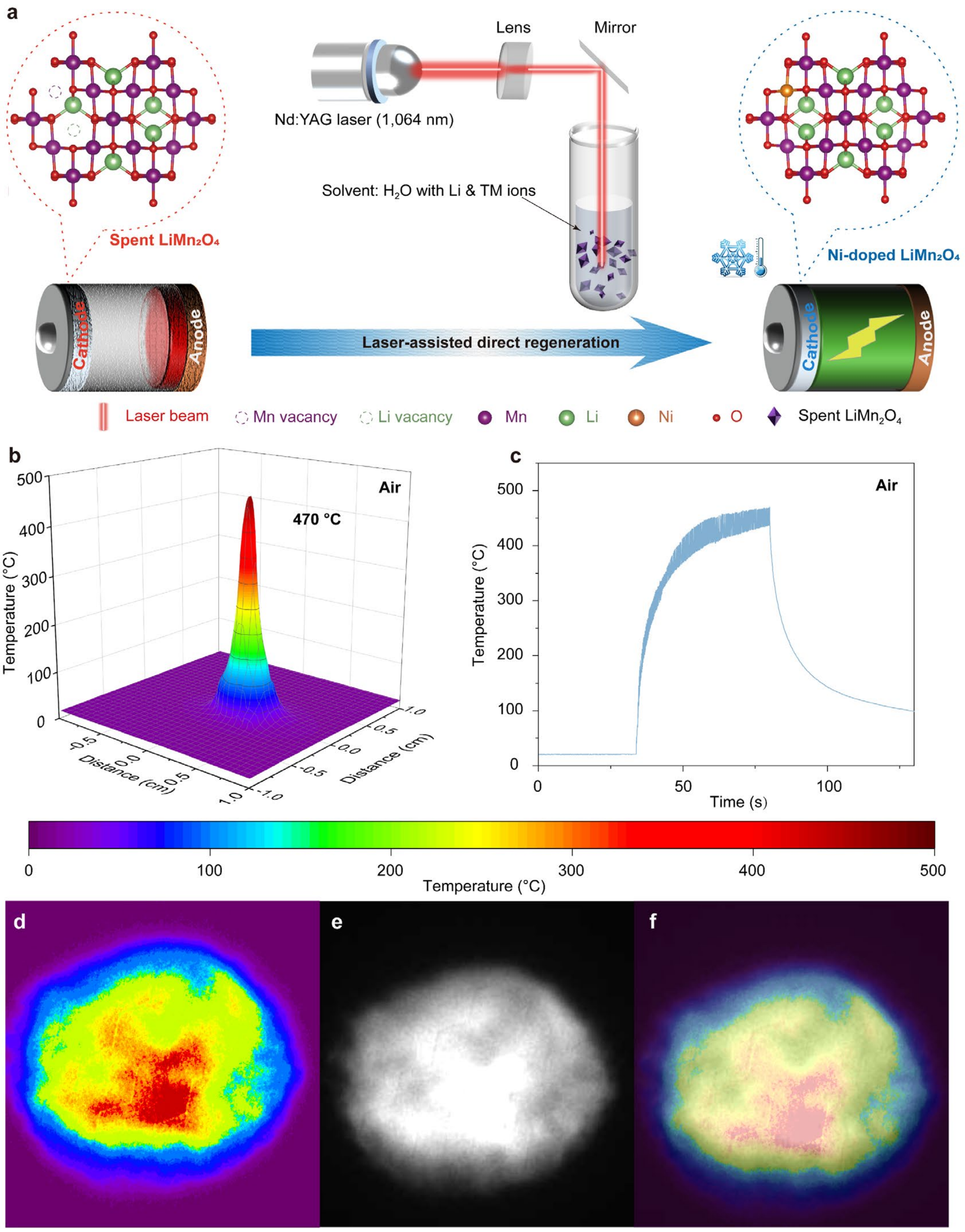

Figure 1. (a) Schematic illustration of laser-assisted direct regeneration strategy of spent $LiMn_2O_4$ cathodes. (b) Temperature distribution and (c) temperature profile of s-LMO during the laser irradiation in air. (d) Infrared thermal image of s-LMO, (e) a photo of laser-induced plasma on s-LMO captured by a high-speed camera, and (f) the corresponding overlay image.

Figure 1a depicts the laser-assisted regeneration process for spent $LiMn_2O_4$ (s-LMO) cathodes. In brief, s-LMO powder was dispersed in an aqueous solution containing Li (2 mM) alone, or a combination of Li with either Ni or Mn (both at 2 mM). The sample regenerated in the solution containing only Li is referred to as r-LMO-Li, while those regenerated in the solution containing both Li and either Ni or Mn are denoted as r-LMO-Ni and r-LMO-Mn, respectively. The regeneration solution was directly irradiated with a Nd:YAG Q-switched pulsed laser (λ = 1,064 nm; 320 mJ) at a 10-Hz repetition rate. The localized high temperatures (up to 470 °C) induced by laser triggers highly active plasma formation (**Figures 1b – c**), which facilitates the regeneration of s-LMO (**Figures 1d – f**). Laser energy is transferred to the solvent molecules, creating high-temperature and high-pressure plasma at the solid–liquid interface.[49–51] This plasma induces the thermal dissociation of bulk s-LMO and generates high-energy particles, which are rapidly quenched by the surrounding solvent. During the quenching process, the composition of LMO is altered, as confirmed by inductively coupled plasma optical emission spectroscopy (ICP-OES, **Table S1**). The Mn/Li molar ratios of r-LMO-Mn (2.00) and r-LMO-Ni particles (1.90) are significantly higher than that of s-LMO (1.77) and r-LMO-Li (1.71).

X-ray diffraction (XRD) patterns of the r-LMO samples were acquired to analyze their crystal structures (**Figure S3**). The XRD pattern of s-LMO confirms $LiMn_2O_4$ as the primary phase, with a minor presence of the Mn_3O_4 phase. Detailed morphological analysis of s-LMO was carried out using scanning electron microscopy (SEM) and transmission electron microscopy (TEM). The s-LMO exhibits an octahedral shape with an average size of approximately 554.70 nm (**Figure S4**). Small particles attached to the s-LMO surface indicate the collapse of the LMO crystal structure likely due to repeated electrochemical cycling and the associated volume changes during Li^+ ion intercalation/deintercalation (**Figure S4b**).[52,53] High-resolution TEM (HRTEM) images presented in **Figures S5a-b** reveal well-resolved lattice fringes of 0.479 nm, corresponding to the (111) plane of LMO. Notably, a crack is evident on the s-LMO surface, extending into the interior (white box in **Figure S5a**), confirming the structural disruption. The observed interplanar spacing of 0.492 nm from the small particles on the s-LMO surface corresponds to the (101) plane of Mn_3O_4 (**Figures S3d-e**), consistent with the XRD patterns and previously reported findings.[36]

X-ray photoelectron spectroscopy (XPS) was conducted to investigate the valence state of the metal species in s-LMO, r-LMO-Mn, and r-LMO-Ni (**Figure S6**). The presence of Mn^{2+} confirms the existence of Mn_3O_4 in s-LMO, indicating that the spinel-structured LMO has been compromised, leading to Li loss during the charge and discharge processes. All regenerated samples exhibit two peaks in the Mn 2*p* region, which are composed of two pairs of Mn^{3+} and

Mn^{4+} species, without any peaks associated with Mn^{2+} species. The Mn^{3+}/Mn^{4+} peak area ratio in s-LMO is calculated as 1.01, which decreases to 0.77 and 0.63 for r-LMO-Mn and r-LMO-Ni, respectively (**Table S2**). This suggests that the laser-assisted regeneration process effectively reduces the proportion of Mn^{3+} in the surface layer, which is linked to Mn dissolution and reduced structural stability. The amount of reagents, chemical composition and valence states of r-LMO samples are optimized by adjusting the PLAL solvent and duration (**Figures S7 – S10** and **Table S3**). Interestingly, the incorporation of transition metals during the PLAL process does not significantly alter the morphology of the r-LMO particles. As observed in the SEM images (**Figure S11**), all r-LMO samples display similar morphologies, with irregular shapes and sizes ranging from several hundred nanometers to 1 μm (average size is approximately 200 nm). Notably, the r-LMO particles are smaller than the s-LMO. This reduction in particle size, which is difficult to achieve using conventional relithiation methods, is a key advantage of the laser-assisted regeneration approach. Smaller particles provide a larger solid–liquid interface area, shortening the migration distance and reducing the energy required for the injection of Li and transition metal ions into s-LMO, thereby facilitating vacancy filling and the regeneration.

The (111) Bragg diffraction peaks of the r-LMO samples shift to lower angles upon the insertion of Li, Ni, and Mn atoms (**Figure S12**). This shift, from 18.65° in s-LMO to 18.64° in r-LMO-Li, is attributed to the reintroduction of Li atoms. Further increases in *d*-spacing are observed for r-LMO-Mn (18.59°) and r-LMO-Ni (18.62°), due to the incorporation of larger Mn and Ni atoms within the crystal structure. (**Figures 2a – d** and **S13**). XRD refinement was conducted to gain further insights into the crystal structures of r-LMO-Mn and r-LMO-Ni (**Figures 2e** and **2f**). All diffraction peaks can be indexed to cubic $LiMn_2O_4$ with the $Fd\bar{3}m$ space group ($a = b = c = 8.22937$ Å, $\alpha = \beta = \gamma = 90°$). Rietveld analysis reveals a slightly smaller lattice parameter for r-LMO-Ni ($a = b = c = 8.22853$ Å, $\alpha = \beta = \gamma = 90°$) compared to r-LMO-Mn (**Table S4**). The incorporation of Ni ions into the $LiMn_2O_4$ structure increases the average valence state of Mn to maintain the electrical neutrality, as confirmed by XPS analysis (**Figure S6**). Consequently, the replacement of Mn^{3+} ($r = 0.645$ Å) with Mn^{4+} ($r = 0.53$ Å) leads to a slight contraction of the unit cell volume.

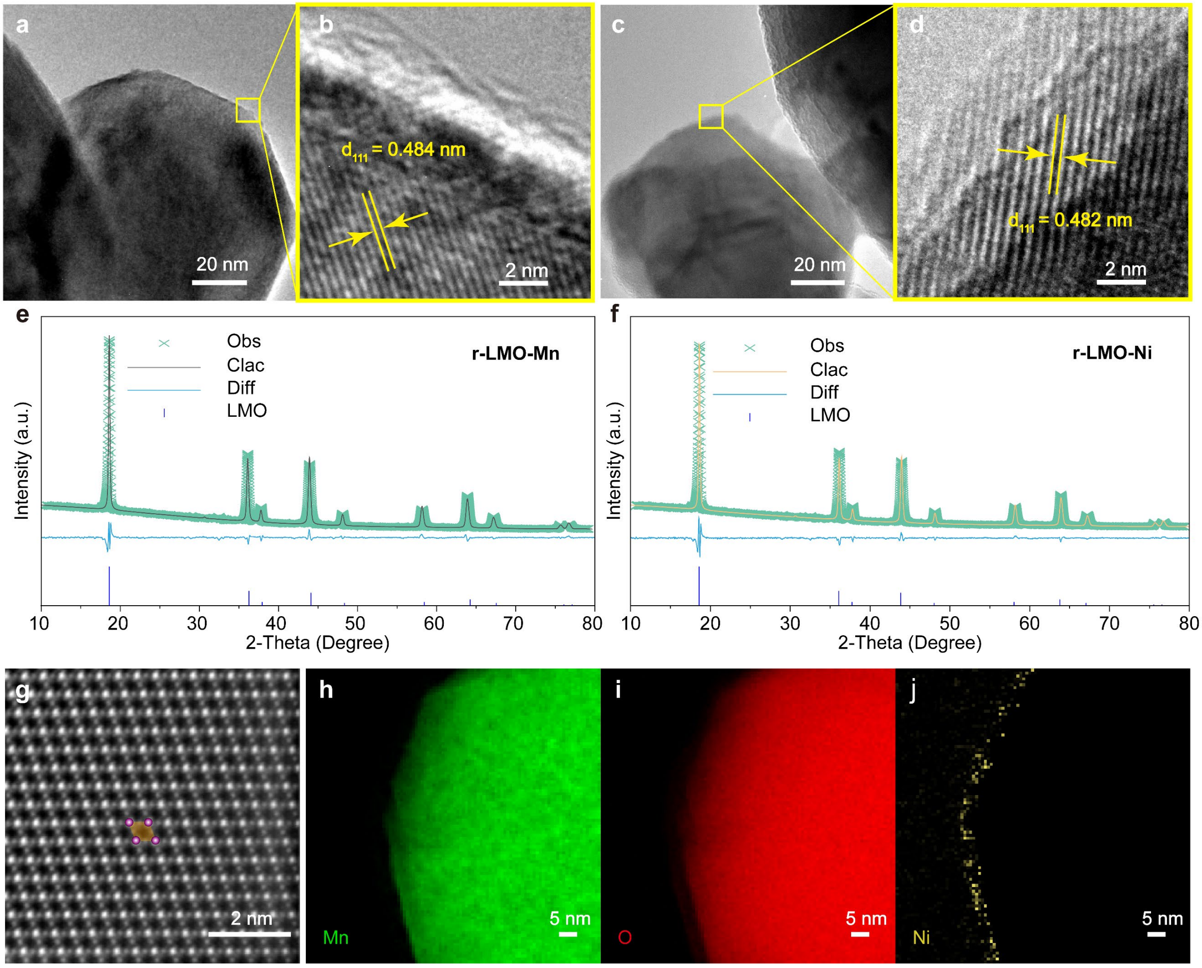

Figure 2. TEM images of (a, b) r-LMO-Mn and (c, d) r-LMO-Ni. XRD refinements of (e) r-LMO-Mn and (f) r-LMO-Ni. (g) AC-STEM image and (h–j) EELS mapping images of r-LMO-Ni.

Aberration-corrected scanning TEM (AC-STEM) equipped with high-angle annular dark-field (HAADF) detectors was employed to directly visualize the impact of Ni doping on the crystallographic structure at the atomic level (**Figures 2g** and **S14**). Notably, the HAADF image of r-LMO-Ni unveils a well-preserved LMO diamond framework, with no apparent occupancy of tetrahedral sites by foreign atoms. This observation suggests that Ni atoms preferentially refill Mn vacancies within the spinel structure. Furthermore, high-resolution energy-loss spectroscopy (EELS) mapping images (**Figures 2h – j**) provide spatially resolved elemental information. The superimposed Mn and Ni signals confirm the presence of Ni primarily on the surface of the regenerated LMO particles. This observation aligns with the proposed regeneration mechanism, where the activated s-LMO interacts with Ni ions at the solid–liquid interface during laser ablation, leading to the formation of r-LMO-Ni with a Ni-doped surface. The incorporation of Ni likely contributes to the improved structural stability of r-LMO-Ni, potentially due to Ni–O bonding within the spinel framework.

2.2. Electrochemical kinetics and performance of r-LMO cathodes

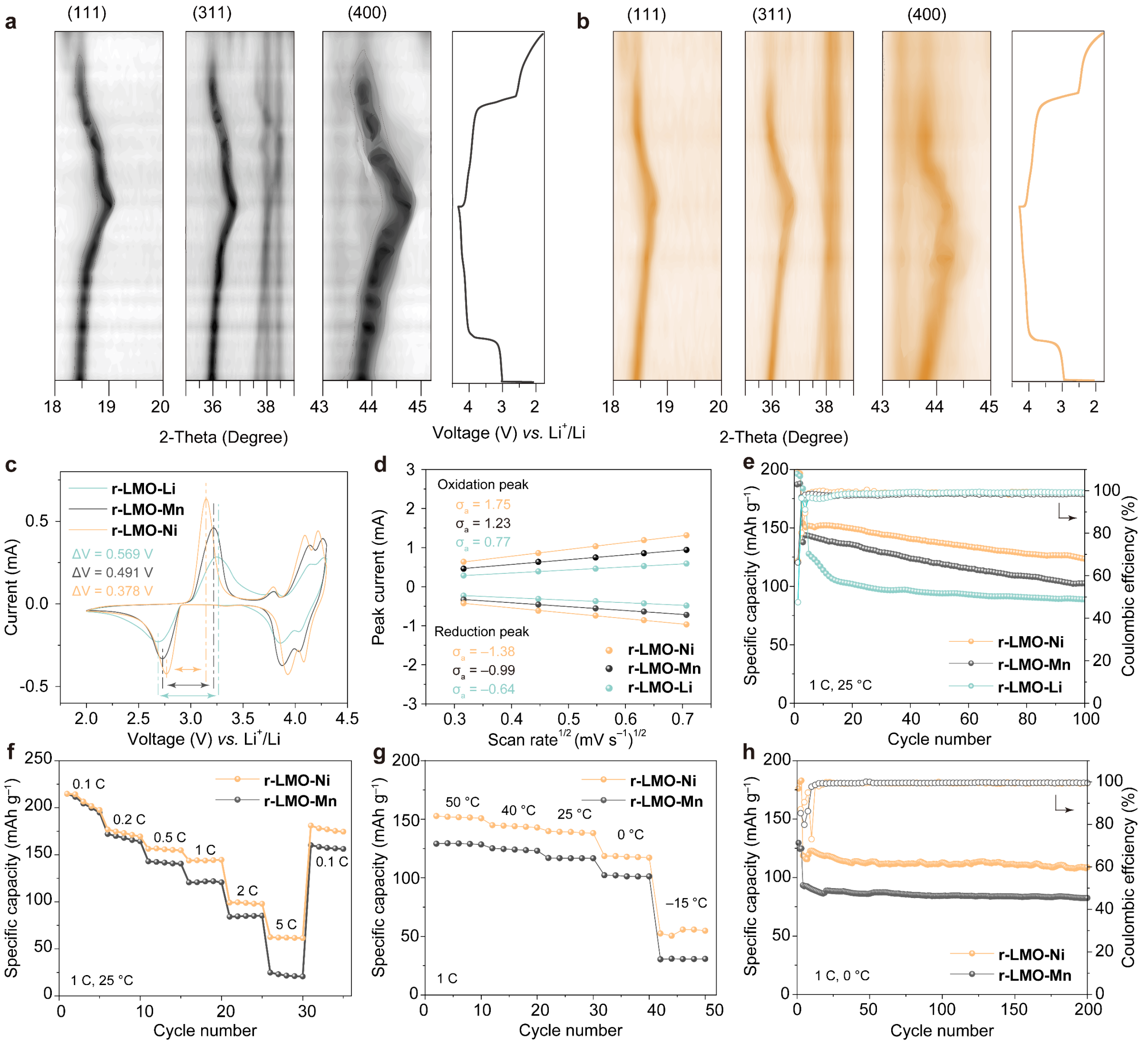

Figure 3. *In situ* XRD patterns of (a) r-LCO-Mn and (b) r-LMO-Ni during a cycle from 2 to 4.3 V *vs.* Li$^+$/Li. (c) CVs (scan rate: 0.1 mV s^{-1}), (d) linear relationships between the major peak current and scan rate, and (e) long cycling performances (1 C under 25 °C) of r-LMO-Li, r-LMO-Mn, and r-LMO-Ni. (f) Rate performances, (g) high and low-temperature performances, and (h) long cycling performances (1 C under 0 °C) of r-LMO-Mn and r-LMO-Ni.

In situ XRD measurements were conducted on r-LMO-Mn and r-LMO-Ni to investigate the impact of Li and Mn supplementation and Ni doping on their structural stability during charge–discharge cycling (**Figures 3a** and **b**). Both samples exhibit distinct shifts in the (111), (311), and (400) Bragg diffraction peaks during cycling. These peak shifts correspond to lattice contraction upon Li de-intercalation and subsequent expansion during Li intercalation. Notably, the magnitude of these peak shifts ($\Delta_{(111)}$, $\Delta_{(311)}$, and $\Delta_{(400)}$) is significantly smaller for r-LMO-Ni (0.34, 0.52, and 0.53) compared to r-LMO-Mn (0.45, 0.80, and 0.84), indicating reduced volume changes in r-LMO-Ni during the electrochemical delithiation/lithiation processes. This smaller volume variation helps to minimize local stress concentration caused by Li insertion/extraction, thereby contributing to the improved long-cycle stability of r-LMO-Ni. *In situ* Raman spectroscopy was also employed to elucidate the surface structural evolution of r-LMO-Mn and r-LMO-Ni during charging (**Figure S12**). The appearance of a spectral peak at 593 cm^{-1}, attributed to the A_{1g} mode of λ-MnO_2, confirms the delithiation process of the cathode and the formation of spinel λ-MnO_2 (space group $F\overline{d}3m$) on the surface. Without Ni and Li supplementation, the spinel structure in LMO is prone to collapse due to Jahn–Teller distortion, resulting in performance degradation.[48]

The potential difference (ΔV) between the reduction and oxidation peaks in the cyclic voltammograms (CVs) reflects the polarization and reversibility of the electrochemical reactions, including the formation of a cathode electrochemical interface (CEI). The ΔV value for r-LMO-Ni (0.378 V) is lower than that of r-LMO-Li (0.569 V) and r-LMO-Mn (0.491 V, **Figure 3c**), indicating reduced polarization and improved electrochemical reversibility for the Ni-doped cathode. This improvement can be attributed to the presence of Ni atoms on the surface, which helps stabilize the spinel structure and reduces drastic volume changes, thus facilitating efficient Li^+ ion diffusion pathways. Furthermore, the calculated Li^+ ion diffusion coefficient in r-LMO-Ni is higher than in r-LMO-Mn and r-LMO-Li (**Figures 3d**, **S16**, and **S17)**, further supporting the notion that surface Ni doping promotes Li^+ ion diffusion. Additionally, electrochemical impedance spectroscopy (EIS) analysis reveals a lower activation energy (E_a) for charge transfer process in r-LMO-Ni electrode (11.3 kJ mol^{-1}) compared to r-LMO-Li (12.2 kJ mol^{-1}) and r-LMO-Mn electrodes (11.5 kJ mol^{-1}, **Figure S18)**. This suggests that surface Ni doping reduces the energy barrier for Li^+ transport across the electrolyte/electrode interface, likely due to changes in interfacial chemistry and the altered ratio of Mn^{4+}–O^{2-} bonds.

The cycling stability of the regenerated samples was evaluated at 1 C (1 C = 148 mAh g^{-1}) and 25 °C (**Figure 3e**). The initial discharge capacity of r-LMO-Li is 127.3 mAh g^{-1}, but it retains only 69.8 % of its initial capacity after 100 cycles. While r-LMO-Mn cathode exhibits a higher initial capacity, greatly exceeding r-LMO-Li, its capacity retention (71.6 %) shows only marginal improvement during prolonged cycling. In contrast, r-LMO-Ni demonstrates superior performance due to surface-doped Ni atoms, with a higher initial capacity (150.51 mAh g^{-1}) and better capacity retention (82.4 %) compared to s-LMO, commercial LMO (c-LMO, **Figure S19)**. The refilling of Li and Mn vacancies in the r-LMO electrodes likely contributes to a higher discharge capacity. Notably, at low current densities (0.1 and 0.2 C), both regenerated cathodes deliver comparable capacities (**Figure 3f**). However, at higher rates, r-LMO-Ni outperforms r-LMO-Mn, indicating enhanced interfacial kinetics from Ni doping.

To assess the impact of Ni doping on electrochemical performance under harsh conditions, r-LMO-Ni and r-LMO-Mn cathodes were tested over a wide temperature range using an environmental chamber (**Figure 3g**). The r-LMO-Ni cathode exhibits remarkable temperature tolerance at a current density of 1 C, delivering higher specific capacities (152.0, 144.5, 139.3, and 118.5 mAh g^{-1} at 50 °C, 40 °C, 25 °C, and 0 °C, respectively) and more stable cycling performance compared to r-LMO-Mn across all temperatures tested. Notably, even at the ultralow temperature of −15 °C, r-LMO-Ni maintains a capacity of 50.5 mAh g^{-1}. Furthermore, unlike conventional approaches that often compromise cycle life for low-temperature performances, r-LMO-Ni demonstrates exceptional stability. Impressively, after 200 cycles at 0 °C (1 C), r-LMO-Ni cathode retains a specific capacity of 112.95 mA h g^{-1} with a capacity retention of 95.1 %, significantly surpassing r-LMO-Mn, c-LMO, and s-LMO (**Figures 3h**, **S20**, and **S21**). These outstanding wide-temperature performance improvements can be attributed to two factors: 1) the laser-assisted regeneration process effectively refills Li and Mn vacancies, enhancing overall capacity and 2) Ni doping alters the interfacial chemistry, reducing the activation energy for charge transfer process, leading to improved performance across a range of temperatures.

2.3. Analysis of doping mechanism and transition metal effect

Figure 4a illustrates the potential Wyckoff positions within the crystal structure of s-LMO, including the 8a site (Li vacancy), the 16d site (Mn vacancy), and the unoccupied 16c site. To determine the most thermodynamically stable sites for Ni atom incorporation, the formation energies associated with Ni occupation at these distinct sites were systematically evaluated using density functional theory (DFT) calculations. Notably, the Mn vacancy site has the lowest formation energy compared to the Li vacancy and 16c empty site (**Figure 4b**), providing a favorable r-LMO-Ni crystal structure model (**Figure S22)**.

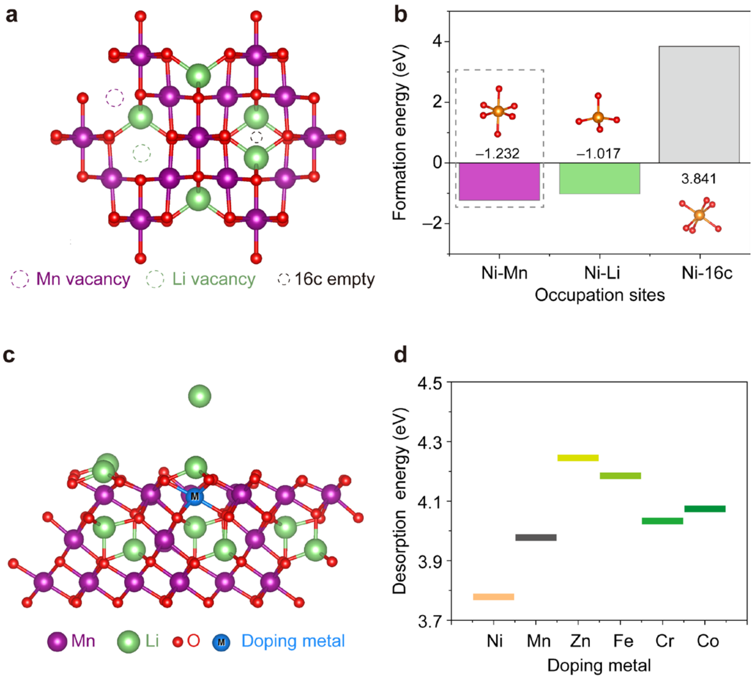

Figure 4. Schematic diagrams showing (a) potential sites for Ni doping inside s-LMO crystal structure and (c) crystal structures of relaxed bare and metal-doped LMO (111) surfaces. (b) Formation energy of Ni doping into different sites. (d) Li desorption energy on the surface of different metal-doped LMO (111).

To explore the influence of various transition metals on the regeneration process, additional metal ions including Zn, Fe, Cr, and Co were incorporated into r-LMO cathodes (r-LMO-TM, TM = Zn, Fe, Cr, and Co) for comparison with r-LMO-Ni. XRD analyses confirm the successful regeneration of the spinel structure, with all diffraction peaks indexed to cubic $LiMn_2O_4$ (F$\bar{d}$3m space group, **Figure S23**). XPS spectra verify the presence of the respective transition metals within the regenerated structures, indicating successful doping (**Figure S24**). Additionally, an increase in the average Mn valence state is observed for all four metal-doped samples compared to the pristine s-LMO. The cycling performance of r-LMO-TM cathodes was evaluated at a current density of 1 C (**Figure S25**). Among the tested samples, r-LMO-Cr displays the most promising performance, delivering a reversible discharge capacity of 67.5 mAh g^{-1} with a capacity retention of 70.1 % after 100 cycles. The other r-LMO-TM cathodes exhibit lower capacities and retention rates: r-LMO-Zn (35 mAh g^{-1}; 35.6 %), r-LMO-Fe (45.5

mAh g^{-1}; 56.3 %), and r-LMO-Co (49.2 mAh g^{-1}; 59.4 %). These results suggest that Ni doping has a more beneficial effect on electrochemical performance compared to doping with Zn, Fe, Cr, or Co (**Figure S26**).

Further DFT calculations were conducted to investigate Li^+ diffusion on the surfaces of different r-LMO-TM samples, as well as r-LMO-Ni and r-LMO-Mn. The calculations focus on the energy required for Li^+ desorption from the surface, as this value is known to determine the overall barrier for both lithiation and delithiation processes (**Figure 4c**).[54] STEM characterizations and DFT calculations indicate that Ni atoms are primarily located within the Mn sites of the r-LMO-Ni surface layer. Compared to other transition metal dopants, Ni offers a unique advantage: it replaces Mn within the MnO_6 octahedral groups while maintaining a favorable energy landscape for Li^+ diffusion (**Figures 4d** and **S27**). This is evident from the DFT calculations, which show a significant reduction (*ca.* 0.2 eV) in the Li^+ desorption energy on the surface upon Ni substitution for Mn. In contrast, other dopants increase the desorption energy, hindering Li^+ diffusion. Combining both experimental and theoretical findings, Ni doping in r-LMO-Ni is believed to offer a synergistic effect: it facilitates Li^+ desorption and promotes Li^+ diffusion within the topmost surface layers, significantly lowering the threshold energy required for interfacial Li^+ transfer processes. This leads to superior electrochemical performance compared to other transition metal dopants.

2.4. Economic and environmental evaluation of laser-assisted direct regeneration strategy

To evaluate the industrial scalability and practicalities of our laser-assisted direct regeneration (LAD) approach for s-LMO cathode, a life-cycle analysis was conducted, considering both environmental and economic factors. This analysis utilized data from the EverBatt model developed by Argonne National Laboratory and Alibaba,[55] reflecting real market prices in China. **Figure 5a** summarizes the current end-of-life battery recycling technologies, including pyrometallurgical (Pyro), hydrometallurgical (Hydro), and LAD routes. Detailed flowcharts for these processes are provided in the supplemental materials (**Figures S28 – S31**).

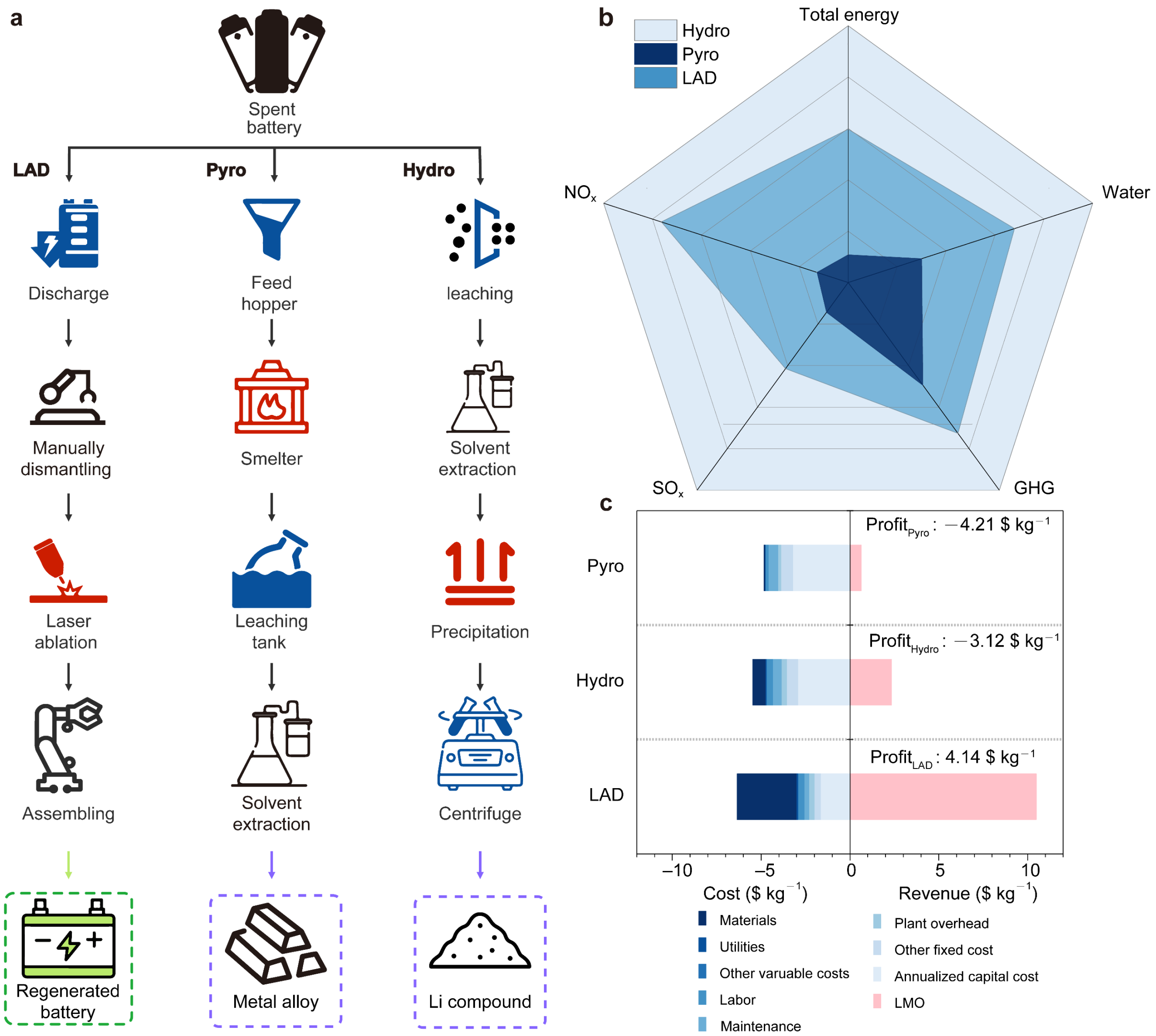

Figure 5. (a) A flowchart showing battery recycling processes, (b) comprehensive comparison, and (c) techno-economic analysis of LAD, Pyro, and Hydro methods.

Figure 5b shows a comprehensive comparison of three recycling methods using a spider chart. The LAD method outperforms hydrometallurgy in terms of greenhouse gas (GHG) emissions, water usage, and total energy consumption. The average total energy consumption for pyro, hydro, and LAD are 4.141, 38.332, and 8.429 MJ kg^{-1} cell, respectively. The life-cycle analysis also considers economic factors, including cost, revenue, and profit, based on an annual processing capacity of 10,000 tons of spent batteries (details in **Tables S5-7**). As shown in **Figure 5c**, the two conventional methods result in negative profits (−4.21 and −3.12 \$ kg^{-1} for pyro and hydro, respectively), making them economically unviable, especially for low-value LMO cells. When assessed in conjunction with the economic benefits, the comprehensive energy–economic benefit of Pyro and Hydro methods are −0.984 and −12.286 MJ $\$^{-1}$, respectively (**Figure S32**). The negative energy-economic benefit is primarily attributed to the low value-added products, such as the Li salt and transition metal oxide, generated by conventional recycling methods. In contrast, our LAD method offers energy–economic benefit of 2.036 MJ $\$^{-1}$. Although this method utilizes expensive chemicals (lithium acetate and nickel acetate) for cathode repair, the high-performance, low-temperature r-LMO-Ni cathode produced offsets this cost. Considering its superior electrochemical performance, reduced environmental impact, and positive economic benefits, laser-assisted regeneration presents a compelling alternative for LMO cathode recycling, offering a promising pathway for profitable and sustainable recycling of LMO batteries.

3. Conclusion

In summary, this work presents a novel laser-assisted regeneration strategy for directly upcycling degraded $LiMn_2O_4$ cathodes. The regenerated cathodes exhibit enhanced low-temperature performance attributed to surface Ni doping. Comprehensive characterizations and analyses reveal that surface chemistry modification through strategic cation doping offers an alternative approach to lowering the energy barrier of the charge transfer process, effectively addressing interfacial limitations that hinder cell operation at low temperatures. Experimental findings and DFT calculations confirm that the improved Li^+ desorption on the surface and Li^+ diffusion within the cathode contribute significantly to these enhancements. As a results, r-LMO-Ni demonstrates exceptional stability, achieving a high capacity of 112.95 mAh g^{-1} (1 C) with remarkable capacity retention (95.1 %) after 200 cycles at 0 °C, outperforming commercial LMO. This work highlights the importance of interfacial engineering in designing LIBs that can operate effectively in low-temperature environments. Furthermore, the straightforward regeneration process and the high added value of r-LMO-Ni indicate its potential for industrial scalability, offering a new paradigm for upcycling spent cathodes and fabricating next-generation Mn-based cathodes.

4. Experimental Section

Details of chemicals, regeneration methods, characterizations, battery performance assessments, *in situ* characterizations, theoretical calculations, and economic and environmental evaluations are presented in the Supporting Information.

Supporting Information

Supporting Information is available from the Wiley Online Library or the author.

Acknowledgements

The authors gratefully acknowledge the financial support from the Hong Kong Polytechnic University, Hong Kong (Q-CDAG) and the Shenzhen Key Basic Research Project, China (JCYJ20220818102210023).

Received: ((will be filled in by the editorial staff))
Revised: ((will be filled in by the editorial staff))
Published online: ((will be filled in by the editorial staff))

4. References

[1] D. Castelvecchi, *Nature* **2021**, *596*, 336.

[2] G. Harper, R. Sommerville, E. Kendrick, L. Driscoll, P. Slater, R. Stolkin, A. Walton, P. Christensen, O. Heidrich, S. Lambert, A. Abbott, K. Ryder, L. Gaines, P. Anderson, *Nature* **2019**, *575*, 75.

[3] X. Lu, Z. Zhang, T. Hiraki, O. Takeda, H. Zhu, K. Matsubae, T. Nagasaka, *Nature* **2022**, *606*, 511.

[4] P. Xu, Q. Dai, H. Gao, H. Liu, M. Zhang, M. Li, Y. Chen, K. An, Y. S. Meng, P. Liu, Y. Li, J. S. Spangenberger, L. Gaines, J. Lu, Z. Chen, *Joule* **2020**, *4*, 2609.

[5] "HONG KONG Waste Rduction Website," can be found under https://www.wastereduction.gov.hk/en-hk/waste-reduction-programme/rechargeable-battery-recycling-programme, **n.d.**

[6] J. Baars, T. Domenech, R. Bleischwitz, H. E. Melin, O. Heidrich, *Nat. Sustain.* **2021**, *4*, 71.

[7] C. Stinn, A. Allanore, *Nature* **2022**, *602*, 78.

[8] E. A. Olivetti, G. Ceder, G. G. Gaustad, X. Fu, *Joule* **2017**, *1*, 229.

[9] B. E. Murdock, K. E. Toghill, N. Tapia-Ruiz, *Adv. Energy Mater.* **2021**, *11*.

[10] M. Iturrondobeitia, C. Vallejo, M. Berroci, O. Akizu-Gardoki, R. Minguez, E. Lizundia, *ACS Sustain. Chem. Eng.* **2022**, *10*, 9798.

[11] Q. Chen, X. Lai, H. Gu, X. Tang, F. Gao, X. Han, Y. Zheng, *J. Clean. Prod.* **2022**, *369*, 133342.

[12] J. J. Roy, B. Cao, S. Madhavi, *Chemosphere* **2021**, *282*, 130944.

[13] B. Makuza, Q. Tian, X. Guo, K. Chattopadhyay, D. Yu, *J. Power Sources* **2021**, *491*, 229622.

[14] Z. Liang, C. Cai, G. Peng, J. Hu, H. Hou, B. Liu, S. Liang, K. Xiao, S. Yuan, J. Yang, *ACS Sustain. Chem. Eng.* **2021**, *9*, 5750.

[15] N. Vieceli, C. A. Nogueira, C. Guimarães, M. F. C. Pereira, F. O. Durão, F. Margarido, *Waste Manag.* **2018**, *71*, 350.

[16] R. Sattar, S. Ilyas, H. N. Bhatti, A. Ghaffar, *Sep. Purif. Technol.* **2019**, *209*, 725.

[17] C. Liu, J. Lin, H. Cao, Y. Zhang, Z. Sun, *J. Clean. Prod.* **2019**, *228*, 801.

[18] S. Natarajan, V. Aravindan, *ACS Energy Lett.* **2018**, *3*, 2101.

[19] Y. Shi, M. Zhang, Y. S. Meng, Z. Chen, *Adv. Energy Mater.* **2019**, *9*, 1900454.

[20] L. A. Diaz, M. L. Strauss, B. Adhikari, J. R. Klaehn, J. S. McNally, T. E. Lister, *Resour. Conserv. Recycl.* **2020**, *161*, 104900.

[21] J. Xu, Y. Jin, K. Liu, N. Lyu, Z. Zhang, B. Sun, Q. Jin, H. Lu, H. Tian, X. Guo, D. Shanmukaraj, H. Wu, M. Li, M. Armand, G. Wang, *Sci. Adv.* **2022**, *8*, 1.

[22] Y. Zhang, J. Li, W. Zhao, T. Yan, L. Zhang, W. Zhang, D. Mei, J. Yu, *J. Am. Chem. Soc.* **2023**, *145*, 27740.

[23] J. Zhou, J. Ni, X. Guan, *RSC Sustain.* **2023**, *1*, 2241.

[24] Z. Li, L. He, Z. W. Zhao, D. Wang, W. Xu, *ACS Sustain. Chem. Eng.* **2019**, *7*, 16738.

[25] J. Piątek, S. Afyon, T. M. Budnyak, S. Budnyk, M. H. Sipponen, A. Slabon, *Adv. Energy Mater.* **2021**, *11*.

[26] J. J. Roy, S. Rarotra, V. Krikstolaityte, K. W. Zhuoran, Y. D. I. Cindy, X. Y. Tan, M. Carboni, D. Meyer, Q. Yan, M. Srinivasan, *Adv. Mater.* **2022**, *34*, 1.

[27] J. B. Dunn, L. Gaines, J. Sullivan, M. Q. Wang, *Environ. Sci. Technol.* **2012**, *46*, 12704.

[28] J. Xiao, J. Li, Z. Xu, *Environ. Sci. Technol.* **2020**, *54*, 9.

[29] W. Gao, X. Zhang, X. Zheng, X. Lin, H. Cao, Y. Zhang, Z. Sun, *Environ. Sci. Technol.* **2017**, *51*, 1662.

[30] G. Ji, J. Wang, Z. Liang, K. Jia, J. Ma, Z. Zhuang, G. Zhou, H. M. Cheng, *Nat. Commun.* **2023**, *14*, 1.

[31] J. Ma, J. Wang, K. Jia, Z. Liang, G. Ji, Z. Zhuang, G. Zhou, H. M. Cheng, *J. Am. Chem. Soc.* **2022**.

[32] K. Jia, J. Wang, Z. Zhuang, Z. Piao, M. Zhang, Z. Liang, G. Ji, J. Ma, H. Ji, W. Yao, G. Zhou, H. M. Cheng, *J. Am. Chem. Soc.* **2022**.

[33] D.-S. Kim, J.-S. Sohn, C.-K. Lee, J.-H. Lee, K.-S. Han, Y.-I. Lee, *J. Power Sources* **2004**, *132*, 145.

[34] J. Chen, Q. Li, J. Song, D. Song, L. Zhang, X. Shi, *Green Chem.* **2016**, *18*, 2500.

[35] T. Wang, H. Luo, Y. Bai, J. Li, I. Belharouak, S. Dai, *Adv. Energy Mater.* **2020**, *10*, 2001204.

[36] J. Lin, E. Fan, X. Zhang, Z. Li, Y. Dai, R. Chen, F. Wu, L. Li, *Adv. Energy Mater.* **2022**, *12*, 1.

[37] J. Wang, K. Jia, J. Ma, Z. Liang, Z. Zhuang, Y. Zhao, B. Li, G. Zhou, H. M. Cheng, *Nat. Sustain.* **2023**, *6*, 797.

[38] P. Xu, Q. Dai, H. Gao, H. Liu, M. Zhang, M. Li, Y. Chen, K. An, Y. S. Meng, P. Liu, Y. Li, J. S. Spangenberger, L. Gaines, J. Lu, Z. Chen, *Joule* **2020**, *4*, 2609.

[39] X. X. Zhao, X. T. Wang, J. Z. Guo, Z. Y. Gu, J. M. Cao, J. L. Yang, F. Q. Lu, J. P. Zhang, X. L. Wu, *Adv. Mater.* **2024**, *2308927*, 1.

[40] X. Chang, M. Fan, B. Yuan, C. F. Gu, W. H. He, C. Li, X. X. Feng, S. Xin, Q. Meng, L. J. Wan, Y. G. Guo, *Angew. Chemie - Int. Ed.* **2023**.

[41] Z. Qin, Y. Zhang, W. Luo, T. Zhang, T. Wang, L. Ni, H. Wang, N. Zhang, X. Liu, J. Zhou, G. Chen, *Angew. Chemie - Int. Ed.* **2023**, *62*.

[42] J. Wang, J. Ma, Z. Zhuang, Z. Liang, K. Jia, G. Ji, G. Zhou, H.-M. Cheng, *Chem. Rev.* **2024**.

[43] E. Fan, L. Li, Z. Wang, J. Lin, Y. Huang, Y. Yao, R. Chen, F. Wu, *Chem. Rev.* **2020**, *120*, 7020.

[44] K. Jia, J. Ma, J. Wang, Z. Liang, G. Ji, Z. Piao, R. Gao, Y. Zhu, Z. Zhuang, G. Zhou, H. Cheng, *Adv. Mater.* **2022**, *2208034*, 2208034.

[45] W. Huang, L. Yang, Z. Chen, T. Liu, G. Ren, P. Shan, B. W. Zhang, S. Chen, S. Li, J. Li, C. Lin, W. Zhao, J. Qiu, J. Fang, M. Zhang, C. Dong, F. Li, Y. Yang, C. J. Sun, Y. Ren, Q. Huang, G. Hou, S. X. Dou, J. Lu, K. Amine, F. Pan, *Adv. Mater.* **2022**, *34*, 1.

[46] S. Zhang, H. Chen, J. Chen, S. Fang, L. Ni, H. Wang, W. Deng, G. Zou, H. Hou, X. Ji, *Adv. Funct. Mater.* **2023**, *33*.

[47] X. Zhu, F. Meng, Q. Zhang, L. Xue, H. Zhu, S. Lan, Q. Liu, J. Zhao, Y. Zhuang, Q. Guo, B. Liu, L. Gu, X. Lu, Y. Ren, H. Xia, *Nat. Sustain.* **2021**, *4*, 392.

[48] W. Zhang, X. Sun, Y. Tang, H. Xia, Y. Zeng, L. Qiao, Z. Zhu, Z. Lv, Y. Zhang, X. Ge, S. Xi, Z. Wang, Y. Du, X. Chen, *J. Am. Chem. Soc.* **2019**, *141*, 14038.

[49] W. Zheng, J. Lee, Z. W. Gao, Y. Li, S. Lin, S. P. Lau, L. Y. S. Lee, *Adv. Energy Mater.* **2020**, *10*, 1.

[50] H. Wang, R. R. Seemakurthi, G. F. Chen, V. Strauss, O. Savateev, G. Hai, L. Ding, N. López, H. Wang, M. Antonietti, *Nat. Commun.* **2023**, *14*, 1.

[51] H. Gao, J. Lee, Q. Lu, Y. Kim, K. H. Shin, H. S. Park, Z. Zhang, L. Y. S. Lee, *Small* **2023**, *19*, 1.

[52] Y. H. Ikuhara, X. Gao, K. Kawahara, C. A. J. Fisher, A. Kuwabara, R. Ishikawa, H. Moriwake, Y. Ikuhara, *ACS Appl. Mater. Interfaces* **2022**, *14*, 6507.

[53] Q. Li, Z. Yao, E. Lee, Y. Xu, M. M. Thackeray, C. Wolverton, V. P. Dravid, J. Wu, *Nat. Commun.* **2019**, *10*, 1.

[54] H. Liang, Z. Ma, Y. Wang, F. Zhao, Z. Cao, L. Cavallo, Q. Li, J. Ming, *ACS Nano* **2023**, *17*, 18062.

[55] Q. Dai, J. Spangenberger, S. Ahmed, L. Gaines, J. C. Kelly, M. Wang, *EverBatt: A Closed-loop Battery Recycling Cost and Environmental Impacts Model,* Argonne National Laboratory*,* **2019** (doi.org/10.2172/1530874).